



**HAL**  
open science

# Enhanced energy, conversion efficiency and collimation of protons driven by high-contrast and ultrashort laser pulses

Weipeng Yao, Ronan Lelièvre, Tessa Waltenspiel, Itamar Cohen, Amokrane Allaoua, Patrizio Antici, Arie Beck, Erez Cohen, Xavier Davoine, Emmanuel D’humères, et al.

► **To cite this version:**

Weipeng Yao, Ronan Lelièvre, Tessa Waltenspiel, Itamar Cohen, Amokrane Allaoua, et al.. Enhanced energy, conversion efficiency and collimation of protons driven by high-contrast and ultrashort laser pulses. *Applied Sciences*, 2024, 14 (14), pp.6101. 10.3390/app14146101 . hal-04797730

**HAL Id: hal-04797730**

**<https://hal.science/hal-04797730v1>**

Submitted on 22 Nov 2024

**HAL** is a multi-disciplinary open access archive for the deposit and dissemination of scientific research documents, whether they are published or not. The documents may come from teaching and research institutions in France or abroad, or from public or private research centers.













L’archive ouverte pluridisciplinaire **HAL**, est destinée au dépôt et à la diffusion de documents scientifiques de niveau recherche, publiés ou non, émanant des établissements d’enseignement et de recherche français ou étrangers, des laboratoires publics ou privés.



Distributed under a Creative Commons Attribution 4.0 International License

## Article

# Enhanced Energy, Conversion Efficiency and Collimation of Protons Driven by High-Contrast and Ultrashort Laser Pulses

Weipeng Yao <sup>1,2,\*</sup>, Ronan Lelièvre <sup>1,3</sup>, Tessa Waltenspiel <sup>1,4,5</sup>, Itamar Cohen <sup>6</sup>, Amokrane Allaoua <sup>3</sup>, Patrizio Antici <sup>5</sup>, Arie Beck <sup>7</sup>, Erez Cohen <sup>7</sup>, Xavier Davoine <sup>8,9</sup>, Emmanuel d'Humières <sup>4</sup>, Quentin Ducasse <sup>3</sup>, Evgeny Filippov <sup>10</sup>, Cort Gautier <sup>11</sup>, Laurent Gremillet <sup>8,9</sup>, Pavlos Koseoglou <sup>12</sup>, David Michaeli <sup>7</sup>, Dimitrios Papadopoulos <sup>1</sup>, Sergey Pikuz <sup>13</sup>, Ishay Pomerantz <sup>6</sup>, Francois Trompier <sup>14</sup>, Yuran Yuan <sup>1</sup>, Francois Mathieu <sup>1</sup> and Julien Fuchs <sup>1,\*</sup>

- <sup>1</sup> LULI—CNRS, CEA, Sorbonne Université, Ecole Polytechnique, Institut Polytechnique de Paris, F-91128 Palaiseau, CEDEX, France; ronan.lelievre@polytechnique.edu (R.L.); tessa.waltenspiel@polytechnique.edu (T.W.); dimitrios.papadopoulos@polytechnique.edu (D.P.); yuran.yuan0324@gmail.com (Y.Y.); francois.mathieu@polytechnique.edu (F.M.)
  - <sup>2</sup> Sorbonne Université, Observatoire de Paris, Université PSL, CNRS, LERMA, F-75005 Paris, France
  - <sup>3</sup> Laboratoire de Micro-Irradiation, de Métrologie et de Dosimétrie des Neutrons, PSE-Santé/SDOS, IRSN, F-13115 Saint-Paul-Lez-Durance, France; amokrane.allaoua@irsn.fr (A.A.); quentin.ducasse@irsn.fr (Q.D.)
  - <sup>4</sup> Centre Lasers Intenses et Applications, University of Bordeaux, CNRS, CEA, UMR 5107, F-33405 Talence, France; emmanuel.dhumieres@u-bordeaux.fr
  - <sup>5</sup> INRS-EMT, 1650 Boul. Lionel-Boulet, Varennes, QC J3X 1S2, Canada; patrizio.antici@inrs.ca
  - <sup>6</sup> The School of Physics and Astronomy, Tel Aviv University, Tel Aviv 6997801, Israel; itamar.oarb@gmail.com (I.C.); ipom@tauex.tau.ac.il (I.P.)
  - <sup>7</sup> Physics Department, NRCN, P.O. Box 9001, Be'er Sheva 8419001, Israel; ariebeck@gmail.com (A.B.); cohen.erez7@gmail.com (E.C.); davidkob@gmail.com (D.M.)
  - <sup>8</sup> CEA, DAM, DIF, F-91297 Arpajon, France; xavier.davoine@cea.fr (X.D.); laurent.gremillet@cea.fr (L.G.)
  - <sup>9</sup> Université Paris-Saclay, CEA, LMCE, F-91680 Bruyères-le-Châtel, France
  - <sup>10</sup> CLPU, 37185 Villamayor, Salamanca, Spain; jienechka@gmail.com
  - <sup>11</sup> LANL, P.O. Box 1663, Los Alamos, NM 87545, USA; gautier@lanl.gov
  - <sup>12</sup> Institute for Nuclear Physics, Technische Universität Darmstadt, Schlossgartenstr. 9, 64289 Darmstadt, Germany; pkoseoglou@ikp.tu-darmstadt.de
  - <sup>13</sup> HB11 Energy Holdings, Freshwater, NSW 2096, Australia; spikuz@gmail.com
  - <sup>14</sup> Laboratoire de Dosimétrie des Rayonnements Ionisants, PSE-Santé/SDOS, IRSN, F-92262 Fontenay-aux-Roses, France; francois.trompier@irsn.fr
- \* Correspondence: yao.weipeng@polytechnique.edu (W.Y.); julien.fuchs@polytechnique.edu (J.F.)



**Citation:** Yao, W.; Lelièvre, R.; Waltenspiel, T.; Cohen, I.; Allaoua, A.; Antici, P.; Beck, A.; Cohen, E.; Davoine, X.; d'Humières, E.; et al. Enhanced Energy, Conversion Efficiency and Collimation of Protons Driven by High-Contrast and Ultrashort Laser Pulses. *Appl. Sci.* **2024**, *14*, 6101. <https://doi.org/10.3390/app14146101>

Academic Editor: Luca Poletto

Received: 27 May 2024

Revised: 28 June 2024

Accepted: 8 July 2024

Published: 12 July 2024



**Copyright:** © 2024 by the authors. Licensee MDPI, Basel, Switzerland. This article is an open access article distributed under the terms and conditions of the Creative Commons Attribution (CC BY) license (<https://creativecommons.org/licenses/by/4.0/>).

**Abstract:** Progress in laser-driven proton acceleration requires increasing the proton maximum energy and laser-to-proton conversion efficiency while reducing the divergence of the proton beam. However, achieving all these qualities simultaneously has proven challenging experimentally, with the increase in beam energy often coming at the cost of beam quality. Numerical simulations suggest that coupling multi-PW laser pulses with ultrathin foils could offer a route for such simultaneous improvement. Yet, experimental investigations have been limited by the scarcity of such lasers and the need for very stringent temporal contrast conditions to prevent premature target expansion before the pulse maximum. Here, combining the newly commissioned Apollon laser facility that delivers high-power ultrashort (~24 fs) pulses with a double plasma mirror scheme to enhance its temporal contrast, we demonstrate the generation of up to 35 MeV protons with only 5 J of laser energy. This approach also achieves improved laser-to-proton energy conversion efficiency, reduced beam divergence, and optimized spatial beam profile. Therefore, despite the laser energy losses induced by the plasma mirror, the proton beams produced by this method are enhanced on all accounts compared to those obtained under standard conditions. Particle-in-cell simulations reveal that this improvement mainly results from a better space–time synchronization of the maximum of the accelerating charge-separation field with the proton bunch.

**Keywords:** high-power lasers; laser-driven ion acceleration; plasma mirror; particle-in-cell simulation

## 1. Introduction

Since their inception in the early 2000s, laser-driven ion beams have opened novel pathways compared to those powered by traditional accelerators [1–3]. Owing to their very compact size ( $\sim 100\ \mu\text{m}$ ), ultrafast timescales ( $\sim\text{ps}$ ), and very high currents ( $\sim\text{kA}$ ) at the source, these beams enable a wide range of applications, spanning flash radiography [4], radiobiology [5], nuclear physics [6], and even ion therapy [7]. They can also be leveraged to generate bright neutron sources [8–11], which already outperform traditional neutron sources in terms of their intensity [12] and hold promise for material probing [13] and astrophysics [14].

Over the past 20 years, research has shown that laser pulses focused at relativistic intensities ( $>10^{18}\ \text{W cm}^{-2}$ ) onto thin solid foils (e.g., a few  $\mu\text{m}$  thick) can generate fast (i.e., up to  $\sim 150\ \text{MeV}$  nowadays [15]) and highly directional ion beams. This process, named target normal sheath acceleration (TNSA) [16], relies on the strong ( $\sim 10^{12}\ \text{V m}^{-1}$ ) electrostatic sheath fields induced by the laser-generated hot electrons [17] at the target surfaces. Typically, TNSA is most efficient at the nonirradiated target backside [18–20], where it produces ion beams with a high particle flux (e.g.,  $\sim 10^{10}$ – $10^{12}$  particles exceeding a few MeV) and a relatively small angular divergence ( $\sim 15$ – $30^\circ$  depending on the energy [21]) [22,23]. Moreover, different kinds of ions can be accelerated simply by changing the target material [24].

Now that we are at the dawn of the multi-petawatt (PW) laser era [25], the vast body of theoretical studies [1,2,26] tells us that further progress should be expected via little-explored, yet likely more efficient ion acceleration processes, i.e., radiation pressure acceleration (RPA) [27–29], breakout-afterburner (BOA) [30], and relativistically induced transparency (RIT) [31–33]. Numerical simulations predict better scaling of the maximum proton energy with laser intensity when utilizing ultrathin (nanometer-range) targets. In experiments, however, triggering the above mechanisms in a controlled way remains very challenging because the amplified spontaneous emission (ASE) pedestal, extending over picosecond or sometimes nanosecond scales ahead of the peak of the laser pulse, can easily preheat or even fully expand the thin target (less than a few microns) [22], resulting in weak or no acceleration at all.

Plasma mirrors (PMs) are a well-known solution to eliminate the ASE and hence to improve the temporal laser contrast, defined as the ratio of the peak intensity to the ASE intensity [34,35]. PMs are commonly made of polished glass slabs or liquid crystals [36] through which the low-intensity ASE light is transmitted. The subsequent rise in laser intensity eventually causes the irradiated PM surface to be ionized and, once the local electron density becomes overcritical, to reflect the main pulse. The resulting higher laser contrast mitigates the formation of a preplasma at the target front, in which the laser can filament [37], and thus allows ultrathin foils to survive until the laser peak, leading to interaction conditions suitable for efficient proton acceleration.

For example, using a PM to achieve a high laser contrast of  $10^{10}$ , laser pulses of 40 fs duration and 1 J energy have been reported to drive protons up to 10 MeV energies from 20–30 nm thick foils [38,39]. Yet, such ultrathin targets tend to result in filamentary proton beam profiles, as compared to the smooth profiles obtained with micrometer-range targets [34,40,41]. Concerning energy conversion efficiency, standard TNSA with  $\sim\mu\text{m}$  thick foils is typically limited to  $\sim 1\%$  efficiency for joule-class lasers [3,40], which can be boosted up to  $\sim 3\%$  if a hybrid TNSA/RPA regime is realized using thinner foils [42]. In the case of nanometer-range liquid crystal targets driven in the RIT regime by 3 J energy, 30 fs laser pulses, 20 MeV proton cutoff energies have been measured, but with degraded beam profile at low proton energy [43].

A general observation is that relatively long (a few 100 fs) pulse durations often lead to poor proton beam quality but higher conversion efficiency [34,41,42]. This is explained by the fact that the ASE-driven expansion of the target increases the plasma density scale length seen by the main laser pulse. This tends to favor the laser absorption into hot electrons but also to disrupt the laser beam profile, entailing, in turn, a degraded imprint in the proton profile. When using a PM, the reduced preplasma due to the higher laser

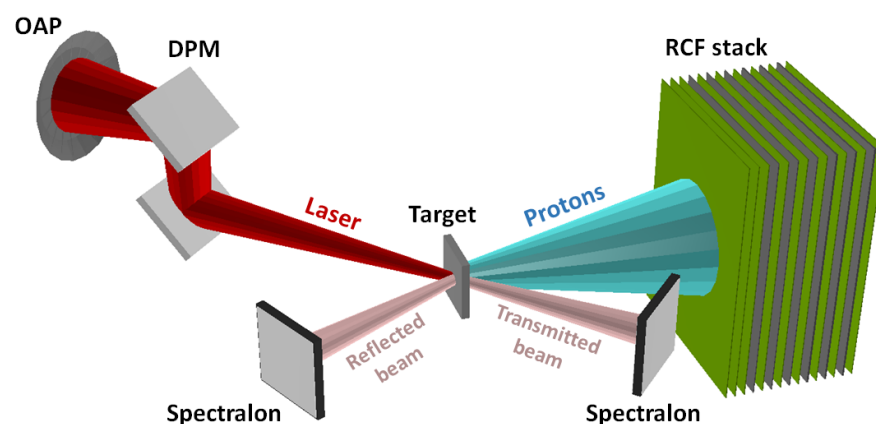
contrast is expected to improve the compactness of the hot-electron distribution and the proton beam quality; yet, the associated laser energy loss, typically around 50%, may detrimentally affect the achievable proton energies. Therefore, it is not clear whether the use of PMs systematically benefits or not proton acceleration.

In this study, we experimentally demonstrate that the combination of an ultrashort ( $\sim 24$  fs) and ultraintense ( $>10^{21}$  W cm $^{-2}$ ) laser pulse with a double plasma mirror (DPM) [34] can significantly improve the maximum energy, conversion efficiency, beam profile, and divergence of the accelerated protons. Numerical particle-in-cell (PIC) simulations support these results, ascribing them to a closer overlap of the maximum of the TNSA field with the front of the proton bunch, where the fastest protons are located. Our findings have important implications for the development of high-quality proton beams for various applications.

## 2. Experimental Setup

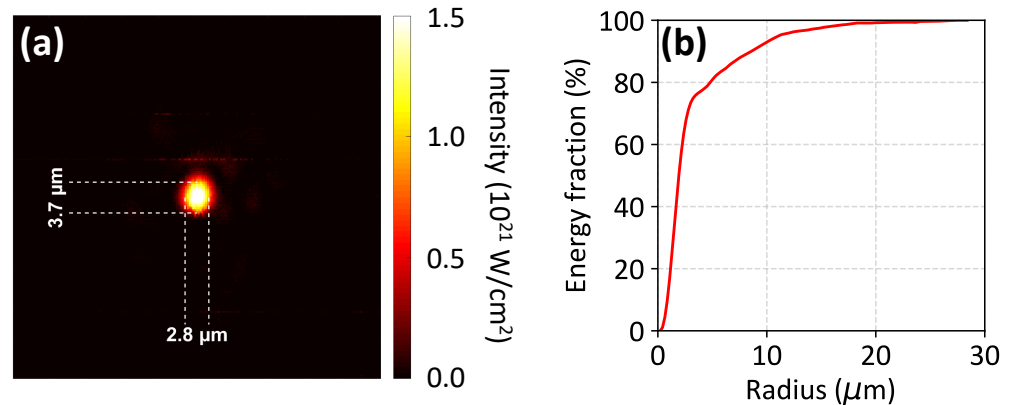
The experiment was performed at the short-focal area of the Apollon laser facility (Saclay, France), using its F2 secondary beam [44]. This beam utilizes a Ti:Sapphire laser, delivering pulses with a full-width-at-half-maximum (FWHM) duration of 24 fs, a mean on-target energy of 11 J, and a central laser wavelength of 815 nm. Two configurations were tested: direct shots (without a DPM) and shots with a DPM [34], in which case the on-target laser energy was reduced to 5.7 J, due to a measured DPM reflectivity of  $\sim 52\%$  reflectivity.

The experimental setup is sketched in Figure 1. The DPM was placed inside the interaction chamber, between the  $f/3$  off-axis parabola (OAP) and the target. The laser focusing used here results from a well-known trade-off: focusing the laser beam too tightly can be detrimental because the energetic electrons escape the laser-heated zone too quickly [45]. Conversely, increasing the focal spot size is generally beneficial for electron heating [46] and ion acceleration [47]. However, for a given laser energy, high intensity from a not-too-tight laser spot is preferable [3], hence our common choice of  $f/3$  focusing. The beam was focused onto the target with a  $45^\circ$  incidence angle. A camera recorded the image of the reflected laser beam on a Spectralon scatter plate positioned along the specular reflection axis (Labsphere, Inc., North Sutton, NH, USA). The transmitted light was monitored by another Spectralon plate placed along the laser transmission axis. Aluminum foils of 0.8–2  $\mu\text{m}$  thicknesses were used on direct shots, while thinner silicon foils, ranging from 10 nm to 300 nm (with, facing the incident laser, an additional coating of 50 nm of Al for some of them, in order to improve the laser absorption and the proton generation [48]), were used with the DPM. The proton spectra were measured using stacks of EBT3 Gafchromic radiochromic films (RCFs) (Ashland Advanced Materials, Bridgewater, NJ, USA) interlaced with aluminum filters, placed at 25 mm from the target.



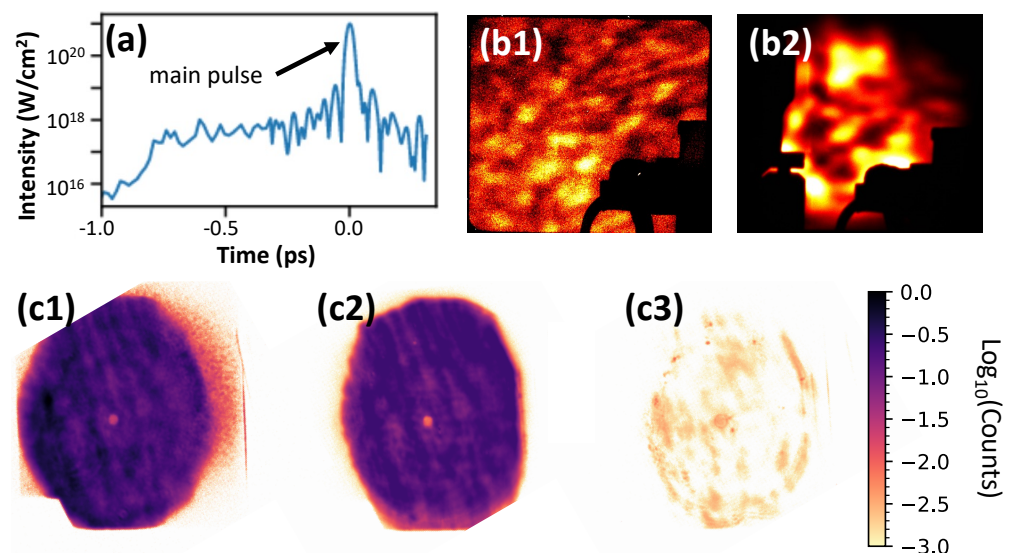
**Figure 1.** Experimental setup. The DPM was positioned between the  $f/3$  off-axis parabola (OAP) and the target. The laser beam hit the target at  $45^\circ$  relative to the target normal. Cameras outside the chamber captured images of the reflected and transmitted laser beams on Spectralon plates. A stack of RCFs (with aluminum filters) was used to measure the proton energy spectrum and spatial profile.

Figure 2 provides information on the focusing of the 140-mm-diameter, near-field laser beam. The focal spot was measured to be elliptical with  $2.8 \mu\text{m} \times 3.7 \mu\text{m}$  FWHM dimensions (see Figure 2a). It contained  $\sim 47\%$  of the on-target laser energy, resulting in a peak intensity of  $\sim 1.5 \times 10^{21} \text{ W cm}^{-2}$ . This peak intensity is evaluated directly from the focal spot image shown in Figure 2a (see caption). These values are very close to those obtained on direct shots during the commissioning of the F2 beam [44], demonstrating that the DPM did not deteriorate the laser focal spot. Figure 2b details the laser energy distribution within the laser spot. The graph plots the fraction of the laser energy within an encircled region as a function of the circle radius from the focal spot center.



**Figure 2.** (a) Laser focal spot measurement (at low power) on a DPM shot. The intensity is calculated from the spatial integration of the energy in each pixel, assuming that the full laser energy is contained in the image and taking into account the laser pulse duration. (b) Encircled laser energy distribution.

The temporal intensity profile of the laser beam (measured without a DPM) is shown in Figure 3a. One can see that before the intensity peak (at time zero), there exists a 750 fs long plateau with a mean intensity of  $\sim 10^{18} \text{ W cm}^{-2}$ . This mildly relativistic intensity level is sufficient to destroy Al targets with thickness below  $1 \mu\text{m}$  [44].



**Figure 3.** (a) Laser contrast measurement during direct (DPM-free) shots. (b) Images of the specularly reflected laser beam collected on a Spectralon plate during a direct shot on a  $1.5 \mu\text{m}$  thick Al target and (b1) a DPM shot on a  $150 \text{ nm}$  (100 nm Si + 50 nm Al) thick target (b2). The shadows present on the images come from objects placed between the target and the Spectralon plate. (c) Images of the transmitted laser beam on another Spectralon plate during DPM shots: (c1) calibration shot (without target), (c2) shot on a  $10 \text{ nm}$  Si foil, and (c3) shot on a  $50 \text{ nm}$  Si foil. Colormaps are normalized to the maximum count in the calibrated shot shown in (c1).

The laser irradiated the PMs at  $45^\circ$  incidence angle, with elliptical spots of dimensions  $\sim 4.5 \text{ mm} \times 6.3 \text{ mm}$  on the PM closest to the focusing OAP and  $\sim 3.5 \text{ mm} \times 5 \text{ mm}$  on the second PM. The peak intensity on the PMs reached  $\sim 5.3 \times 10^{13} \text{ W cm}^{-2}$ , while the prepulse plateau intensity was  $\sim 2.6 \times 10^{10} \text{ W cm}^{-2}$ . These values are, respectively, well above and below the ionization threshold ( $\sim 2.5 \times 10^{12} \text{ W cm}^{-2}$ , considering the  $\sim 750 \text{ fs}$  prepulse duration) of the fused silica material of the PM [49]. The on-target intensity contrast between the prepulse plateau and pulse maximum was then increased by the square of the ratio between the reflection factor of the ionized PM ( $\sim 0.52$ ) and the antireflection coating factor of each PM ( $\sim 10^{-3}$ ), i.e., by a factor of  $\sim 2.7 \times 10^5$ . This would bring the prepulse plateau intensity down to  $\sim 4 \times 10^{12} \text{ W cm}^{-2}$ , causing minimal, if any, disturbance to the foil targets. This prediction is supported by the observed smooth spatial profiles of the protons accelerated from targets as thin as  $20 \text{ nm}$  (see below). These profiles exhibit no modulations, in contrast to previous findings [34,40,41]. This difference may be linked to the fact that the latter studies employed longer laser pulses than ours, leaving more time for the target surface to deform during ion acceleration.

Figure 3(b1) shows a typical image of the specularly reflected beam, as obtained on the Spectralon plate without a DPM. The beam profile appears to be diffuse and of low intensity, meaning that the laser beam was reflected off an extended preplasma, as a result of the prepulse-induced target expansion. By contrast, the reflected beam profiles recorded on DPM shots (see Figure 3(b2)) were much more intense and collimated, suggesting that the laser interacted with a sharp target surface. This behavior is consistent with previous experiments using DPMs [39,43].

Figure 3(c1) displays the transmitted laser beam profile measured with a DPM in the absence of a target. A very similar image (Figure 3(c2)), associated with a laser transmission rate of  $\sim 88\%$ , was recorded when shooting at the thinnest ( $10 \text{ nm}$ ) Si foils, in which case no proton acceleration was detected. This indicates that, despite the enhanced contrast achieved by the DPM, such ultrathin targets remain vulnerable to the ASE. However, when the target thickness was increased to  $50 \text{ nm}$ , fast protons were measured up to  $\sim 20 \text{ MeV}$  while the laser transmission rate plummeted to  $\sim 0.5\%$  (see Spectralon image in Figure 3(c3)).

### 3. Experimental Results

#### 3.1. Increased Proton Energies

The proton energy spectra were inferred from the doses deposited into the RCF stack as detailed in Ref. [21]. Figure 4a shows two proton spectra for the target thicknesses maximizing the proton cutoff energy ( $E_{\text{max}}$ ) with or without a DPM. Overlaid are predictions from PIC simulations (see Section 4).

The best performance in the no-DPM case was recorded with a  $1.5 \mu\text{m}$  thick Al foil, yielding  $E_{\text{max}} \simeq 25 \text{ MeV}$ . The best DPM shot used a  $250 \text{ nm}$  ( $200 \text{ nm Si} + 50 \text{ nm Al}$ ) thick foil, yielding  $E_{\text{max}} \simeq 35 \text{ MeV}$ , i.e., a  $\sim 40\%$  enhancement. The proton spectra plotted in Figure 4a exhibit an exponential behavior of the form  $dN/dE = (N_p/T_p) \exp(-E/T_p)$  for  $E \leq E_{\text{max}}$ , where  $E$  is the proton energy,  $T_p$  the effective temperature and  $N_p$  the total proton number. The best-fitting parameters are  $N_p = 2.1 \times 10^{11}$  and  $T_p = 3.0 \text{ MeV}$  without the DPM, and  $N_p = 1.4 \times 10^{11}$  and  $T_p = 4.0 \text{ MeV}$  with the DPM. Note that the first RCFs were excluded from the analysis because their signal was saturated and they did not collect a fraction of the proton beam (the lateral extent of the proton beam exceeds the size of the films for these first layers, as shown in the raw RCF data below). The low-energy ( $< 8 \text{ MeV}$ ) component of the proton spectra not captured by the RCFs was characterized by a magnetic spectrometer in a previous campaign, conducted under similar interaction conditions, but without a DPM [50]. This measurement revealed a steeper proton spectrum ( $T_p \simeq 1.1 \text{ MeV}$ ).

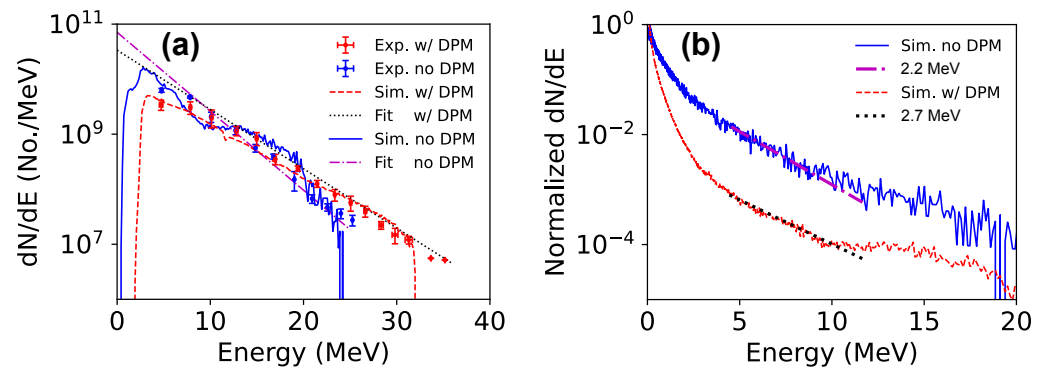


**Figure 4.** (a) Measured proton spectra, extracted from RCF data in the DPM case with a 250 nm (200 nm Si + 50 nm Al) thick target (red points, averaged over 3 shots) and in the no-DPM case with a 1.5  $\mu\text{m}$  thick Al target (blue points, averaged over 2 shots). Error bars represent the minimum and maximum values from different shots with the same target thickness. Exponential fits are shown as black dotted lines (DPM case) and purple dashed-dotted lines (no-DPM case). 2D PIC simulation results for both cases are plotted as red dashed and blue solid lines, respectively. (b) Simulated electron spectra together with exponential fits in the 4.5–11.5 MeV range. The line styles are the same as in panel (a).

Figure 5a shows how the proton cutoff energy varies with target thickness ( $d$ ). Empty and filled symbols represent the maximum and mean cutoff energies, respectively, from all shots with a given target thickness. Both quantities exhibit the same behavior, peaking around  $d = 250$  nm with a DPM and at  $d = 1.5 \mu\text{m}$  without. Notably, in the absence of a DPM, no detectable proton signal is observed from Al targets thinner than 800 nm. With a DPM, significant proton acceleration is achieved even in Si foils as thin as 20 nm, with a maximum proton energy of around 15 MeV.

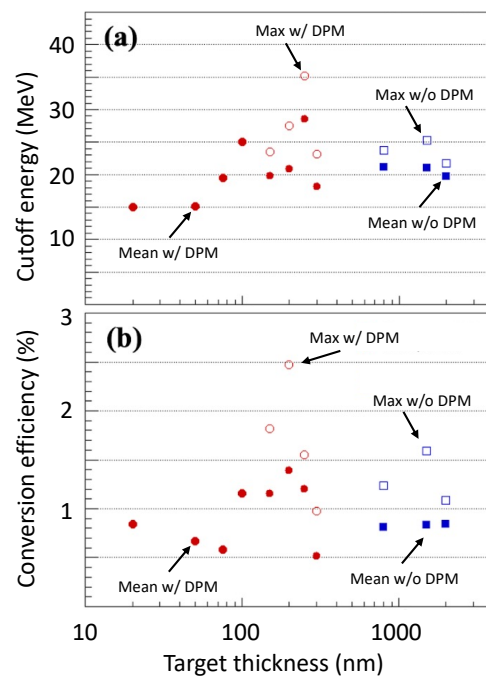


**Figure 5.** Target thickness dependence of the (a) proton cutoff energy and (b) laser-to-proton energy conversion efficiency (see text for definition). For both quantities, we distinguish between the maximum (empty symbols) and mean (filled symbols) values for all shots performed with the same target thickness. Direct and DPM shots are represented by squares and dots, respectively. The target thickness for DPM shots refers to the entire Si/Al target. For the thinnest targets, the results are single-shot, hence no mean is reported.

Figure 5b shows the conversion efficiency of laser energy into protons, evaluated by integrating (over  $0 \leq E \leq E_{\max}$ ) the exponential fit of each recorded proton spectrum (see Figure 4a). We use the fit of the spectrum rather than the actual spectrum since, as discussed above, the number of low-energy protons retrieved from the first films is underestimated (the films are saturated). The laser energy considered here is the on-target value for each configuration (i.e., taking into account the energy loss induced by the DPM). As in Figure 5a, we distinguish between the maximum and mean values obtained for a given target thickness. The dependence of both quantities on target thickness is similar to that observed for the proton energies, i.e., adding the DPM leads, for the best cases, to an increase in the maximum (resp. mean) conversion efficiency by 56% (resp. 75%), i.e., from 1.6% to 2.5% (from 0.8% to 1.4%). The conversion efficiencies recorded here for TNSA protons are on par, i.e., in the few percent range, with what has been measured in other ion acceleration regimes, e.g., RPA [51,52].

Interestingly, for the DPM shots, the observed drop in proton cutoff energy and conversion efficiency with decreasing target thickness below  $d = 250$  nm is gentler than in previous studies using longer laser pulses. Specifically, the decrease is  $\sim 0.54$  for the cutoff energy (from 30 MeV to 15 MeV) and  $\sim 0.47$  for the conversion efficiency (from 1.4% to 0.8%) as the target thickness is reduced from  $d = 250$  nm to  $d = 20$  nm. These values are comparable to those reported in Ref. [40] with a 35 fs pulse (0.31 for cutoff energy and 0.59 for efficiency, for thicknesses from 20 to 100 nm) but significantly lower than those obtained with a 900 fs pulse in Ref. [42] (0.67 for cutoff energy and 0.79 for efficiency, for thicknesses from 10 to 100 nm). The smaller decrease obtained in our case with ultrahigh-contrast, ultrashort pulses indicates a more robust acceleration scheme, because even ultrathin targets (down to  $d = 20$  nm here) do not have time to fully expand before the laser intensity peaks, resulting in a sustained “plateau” in the performance metrics. A similar plateau behavior in proton acceleration has been reported in Refs. [38,43].

To summarize this section, our main finding is that, despite reducing the on-target laser energy by almost a factor of 2, the use of a double plasma mirror (DPM) leads to a significantly (by  $\sim 40\%$ ) higher proton cutoff energy, but is accompanied by a loss of low-energy protons (see Figure 4a). It is also worth noting that, in the same experiment, very similar neutron yields from  $(p, n)$  nuclear reactions were detected in both direct and DPM shots [11].

As will be detailed below, the enhanced ion acceleration in high-contrast laser-foil interactions originates from a close overlap of the peak accelerating electric field with the proton bunch. A similar interpretation was put forward to explain the strong increase in the conversion efficiency observed when relatively thick ( $d = 5 \mu\text{m}$ ) targets were irradiated by two sequential ps-long laser pulses [53].

### 3.2. Improved Proton Beam Profile

Another benefit of the DPM is the significant improvement in the proton beam profile. Figure 6 compares the raw RCF data from direct and DPM shots. The spatial dose distribution at low proton energy ( $\lesssim 11$  MeV) proves to be much wider with a DPM (middle and bottom rows) than without it (top row). In the latter case, the distribution exhibits two components, one along the laser axis (red arrow) and one along the target normal (black arrow), as previously observed in Ref. [54]. With the DPM, however, the beam profile is preferentially concentrated around the target normal.

At higher proton energy, the beam profile becomes filamentary in the absence of a DPM, while it retains a rather collimated and round shape with a DPM. This trend, which differs from previous measurements [41], still holds in foils as thin as 20 nm (bottom row), likely a consequence of the shorter pulse duration used in our experiment, which minimizes the target pre-expansion. This may have important implications for proton radiography [4], where a smooth profile translates into better image quality, and for medical applications that necessitate homogeneous irradiation profiles [5,7].



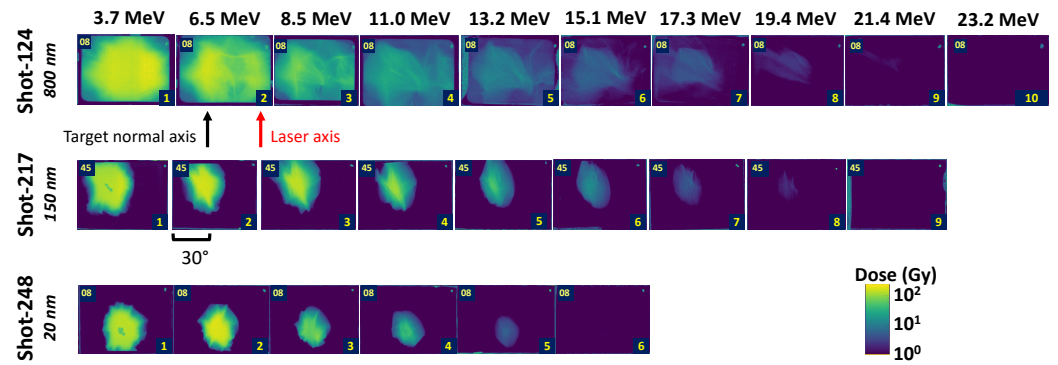


**Figure 6.** Spatial dose distribution on the RCF stack. (**Top row**) No-DPM shot on a 800 nm thick Al target. (**Middle row**) DPM shot on a 150 nm (100 nm + 50 nm Al) thick target. (**Bottom row**) DPM shot on a 20 nm thick Si target. The first two shots yield similar maximum proton energies, but different spatial beam profiles. The same colormap is used in all images. The arrows locate the laser propagation direction (red) and the target normal (black) direction. The marks on the films are used for traceability: the number on the top left is the shot sequence number, the one on the bottom right is the number of the film in the stack. The last film, void of visible proton beams, is shown to demonstrate that the proton beam cutoff corresponds to the second to last film in the stack.

The nonuniform profile of the proton beam produced without a DPM is attributed to the extended low-density plasma created by the laser prepulse. This preplasma causes the main pulse to filament, which affects the hot-electron distribution and ultimately the angular profile of the accelerated protons. In contrast, when a DPM is used, the laser interacts directly with the sharp surface of the solid target, likely resulting in a more homogeneous hot-electron profile.

Figure 7 quantifies the improved beam collimation achieved with the DPM. It shows the half-width of the beam angular distribution for the same shots discussed previously, as a function of energy normalized to the respective maximum cutoff energy. We observe a significantly wider divergence for direct shots, with angles exceeding 20° at low energies and remaining above 10° at high energies. The error bars of the data are compatible with the expected energy-dependent divergence of TNSA protons [21], plotted as a black curve. However, the DPM shots on 20 nm and 150 nm thick foils give much smaller divergence angles, consistent with Ref. [38]. These angles decrease from ~12° at low relative energy ( $E/E_{max} \sim 0.2$ ) down to ~5° near the cutoff energy.

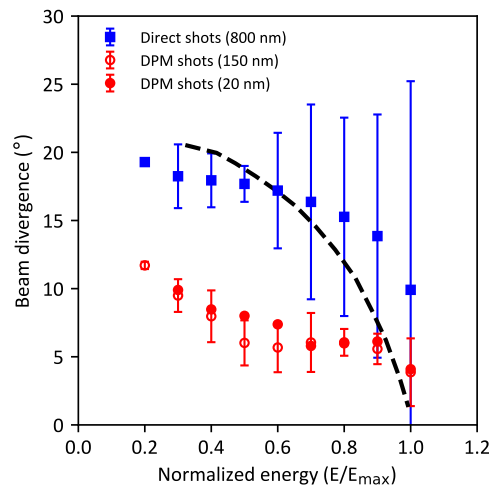


**Figure 7.** Measured half-width of the proton angular distribution as a function of proton energy (normalized to the cutoff energy). Filled blue squares: direct shots on 800 nm thick Al foils (symbols represent the average values and error bars the maximum and minimum values over the considered

series of shots). Filled red circles: DPM shots on 150 nm (100 nm Si + 50 nm Al) thick foils. Empty red circles: DPM shots on 20 nm thick Si foils. The black dashed curve represents the energy-dependent angular distribution observed in many experiments to be characteristic of TNSA protons [21].

### 3.3. X-ray Emission

The X-ray emissions from the laser-foil interactions were measured with two diagnostics: a set of dosimeters with broad spectral sensitivity [55] and a spatially resolved spectrometer working in the keV range [56].

Twenty GD-351 radio-photo-luminescence dosimeters [55] were placed at various angles and positions inside the interaction chamber, at distances ranging from 87 cm and 115 cm from the target. The dosimeters were encapsulated in a 1.5 mm thick tin holder, making them sensitive to X-rays in an energy range from around 30 keV to a few MeV, with an energy-independent response. The tin holder also served to protect the dosimeters from protons up to 23 MeV and electrons up to 1.5 MeV, by absorbing these particles, preventing them from depositing their energy into the dosimeters. However, in the absence of comparative measurements of the X-ray and electron energy spectra, we cannot exclude the possibility that higher-energy electrons contributed to the dosimeter signal.

Taking advantage of the high repetition rate of the Apollon laser, the dosimeter signals were accumulated over several shots (typically 20), enabling comparisons between different sessions by averaging out laser fluctuations. Figure 8 depicts two representative dose distributions obtained with direct and DPM shots, revealing strong differences between the two configurations. For direct shots (left panel), the doses are preferentially delivered in a broad lobe that extends between the target normal and the laser specular reflection axis. By contrast, the DPM shots (right panel) result in a much narrower emission cone centered along the laser specular direction. We also observe significant dose emission along the rear target normal in direct shots, which is absent with the DPM. Specifically, a factor of up to 130 is measured between the doses emitted in the backward direction for direct and DPM shots, with approximately 1670  $\mu\text{Gy}$  and 12.8  $\mu\text{Gy}$  per shot, respectively.

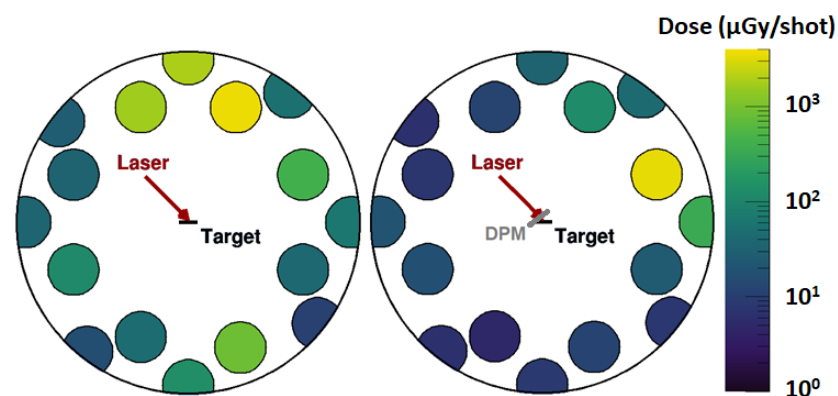


**Figure 8.** Spatial dose distribution recorded inside the interaction chamber by a set of dosimeters (details in text). **Left panel:** results for direct shots on Al foils of 0.8  $\mu\text{m}$ , 1.5  $\mu\text{m}$  and 2  $\mu\text{m}$  thicknesses. **Right panel:** results for DPM shots on Si/Al foils of 150 nm, 200 nm and 250 nm thicknesses. Each circle represents a dosimeter, and its color corresponds to the measured dose. The outer circle in both graphs represents the actual diameter of the target chamber. The gray bar representing the DPM in the right panel is to scale.

The broad angular distribution and high doses observed in the direct shots are consistent with dominant Bremsstrahlung emission. This is likely due to the presence of a significant preplasma at the target front, where laser-driven electrons can recirculate and radiate [57,58]. In contrast, the significant reduction in dose and the directional nature of the X-ray emission in the DPM case suggest a different radiation generation mechanism. The thinner targets used with the DPM reduce the hot-electron path length in matter,

thereby decreasing the probability of Bremsstrahlung. Furthermore, in high-contrast, oblique laser-solid interactions such as those with the DPM, electrons can be accelerated along the target surface to high energies, radiating predominantly in the near-surface direction [59,60]. In addition, the laser beam reflected off the solid surface can directly accelerate some electrons [61], possibly leading to X-ray emission through betatron oscillations. Both mechanisms align well with the observed narrow cone of emission in the DPM case (Figure 8).

We now consider the spatially resolved measurements of the X-ray source. The focusing spectrometer [56], directed at the target front along the target normal, measured the K-shell emission of the plasma in the 1500–2000 eV range (wavelengths  $\lambda = 6.4\text{--}8\text{ \AA}$ ). A mica crystal was used in the second order of reflection ( $2d = 19.9419\text{ \AA}$ ) to measure the spectral lines of aluminum ( $\text{Ly}\alpha$ ,  $\text{He}\beta$ , and  $\text{He}\alpha$  with their satellites) and silicon ( $\text{He}\alpha$  with its satellites if present). The emission was recorded on a TR-type image plate. The spatial resolution of the measurement was  $200\text{ }\mu\text{m}$ , limited by the combined effects of the Fujifilm BAS-1800 II scanner resolution and the demagnification of the optical scheme. To protect the image plate from optical radiation, the detector holder was covered with an aluminized polypropylene foil ( $2\text{ }\mu\text{m}$  PP +  $80\text{ nm}$  Al).

Figure 9 shows a typical X-ray spectrum averaged over seven DPM shots on  $200\text{ nm}$  Si foils with a  $50\text{ nm}$  Al coating (on the laser-irradiated side). By contrast, spectra without DPM exhibited strong noise, making it impossible to distinguish spectral lines. The fact that the lines in the spectrum can be distinguished from the background in the DPM case likely originates from a lower contribution from continuum emission. The latter can be attributed to both the higher laser contrast (the target being then not pre-expanded into a large volume low-density plasma, as is the case in the direct shots) and the different X-ray generation mechanisms discussed above. The spectrum shown in Figure 9 contains mostly the X-ray emission of aluminum with only a minor contribution from silicon near the Al  $\text{He}\beta$  and Li-like emission ( $6.4\text{--}6.9\text{ \AA}$ ). Thus, the effective (i.e., temporally averaged over the plasma expansion and spatially averaged over the spectrometer's line-of-sight) electron density ( $n_e$ ) and temperature ( $T_e$ ) of the emitting plasma can be inferred through comparison to FLYCHK atomic physics calculations [62] of aluminum. As shown in Figure 9, the best-fitting parameters are  $n_e = 3 \times 10^{22}\text{ cm}^{-3}$  and  $T_e = 350\text{ eV}$ . These values demonstrate the ability of the DPM to maintain the integrity of the ultrathin foils until the pulse maximum.

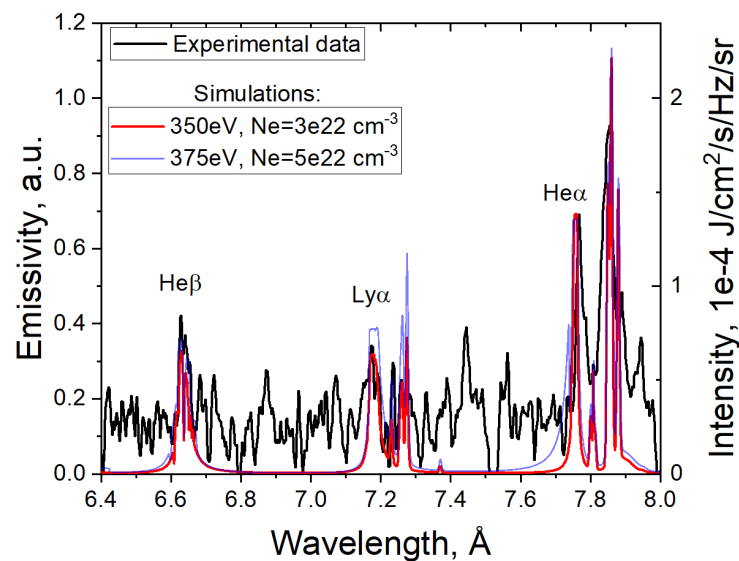


**Figure 9.** X-ray spectra averaged over seven DPM shots on a  $200\text{ nm}$  Si foils with a  $50\text{ nm}$  Al coating (on the laser-irradiated side) (black curve). The red and blue curves represent FLYCHK atomic physics calculations for Al emission at  $n_e = 3 \times 10^{22}\text{ cm}^{-3}$  and  $T_e = 350\text{ eV}$ , and  $n_e = 5 \times 10^{22}\text{ cm}^{-3}$  and  $T_e = 375\text{ eV}$ , respectively.

#### 4. Numerical PIC Modeling

To elucidate the mechanism behind the enhanced proton acceleration with a DPM, we have carried out 2D PIC simulations with the fully relativistic and electromagnetic SMILEI code [63]. The numerical domain has dimensions of  $L_x \times L_y = 21 \times 42 \mu\text{m}^2$  with a mesh size  $\Delta x = \Delta y = 7.8 \text{ nm}$ , corresponding to 128 cells per micron. The time step is  $\Delta t = 0.5\Delta x/c$ , where  $c$  is the speed of light. The laser beam, of wavelength  $\lambda_0 = 0.8 \mu\text{m}$ , is injected from the lower left side ( $x = 0$ ) of the box at  $45^\circ$  incidence angle. It is focused with  $p$ -polarization onto the front side of the target (at  $x = 10 \mu\text{m}$  and  $y = 21 \mu\text{m}$ ). It has a Gaussian envelope with  $3 \mu\text{m}$  FWHM spot size and 24 fs FWHM duration. In the no-DPM case, the laser peak intensity is  $I_0 = 1.8 \times 10^{21} \text{ W cm}^{-2}$ , corresponding to  $a_0 = 29.2$ . The laser beam also has a 1 ps long prepulse with the same spatial profile and a constant intensity. The intensity of the prepulse was adjusted so that the simulated proton energy spectrum matches the experimental one, see Figure 4a. In the DPM case, we consider only the main 24 fs pulse, with no prepulse, but with a reduced peak intensity of  $9 \times 10^{20} \text{ W cm}^{-2}$  (corresponding to  $a_0 = 20.5$ ) to take into account the energy loss associated with the DPM.

In the no-DPM case, the plasma targets consist of neutral Al foils with thickness  $d = 0.8\text{--}2 \mu\text{m}$ . In the DPM case, we use neutral Si foils with  $d = 10\text{--}300 \text{ nm}$ , followed by a 50 nm thick neutral Al layer. All targets are coated with a 10 nm thick hydrogen contaminant layer on their backside. Due to computational limitations, their initial ion number density is capped at a sub-solid density value, i.e.,  $n_i = 60 n_c$ , where  $n_c = m_e \epsilon_0 \omega_0^2 / e^2 = 1.75 \times 10^{21} \text{ cm}^{-3}$  is the critical density at the laser wavelength  $\lambda_0 \equiv 2\pi c / \omega_0$  ( $\epsilon_0$  is the vacuum permittivity,  $m_e$  the electron mass, and  $e$  the elementary charge). Electron and ion species are represented by 256 macroparticles per cell, with a fourth-order shape-function. All simulations describe field and electron impact induced ionization. Boundary conditions for both particles and fields are open along both longitudinal ( $x$ ) and transverse ( $y$ ) directions. The integration time of the simulations is 500 fs after the laser peak.

To illustrate the coupling of the prepulse-free laser (DPM case) with two ultrathin Si foils as a function of their thickness, we display in Figure 10 the spatial distribution of the transverse electric field ( $E_y$ ). We observe near-complete laser transmission across the 10 nm target (Figure 10a) while the 20 nm target gives rise to partial transmission and reflection (Figure 10b). This behavior aligns with our experimental findings, i.e., high laser transmission across the 10 nm foil (Figure 3(c2)) and no detectable protons for targets thinner than 20 nm (Figure 5).

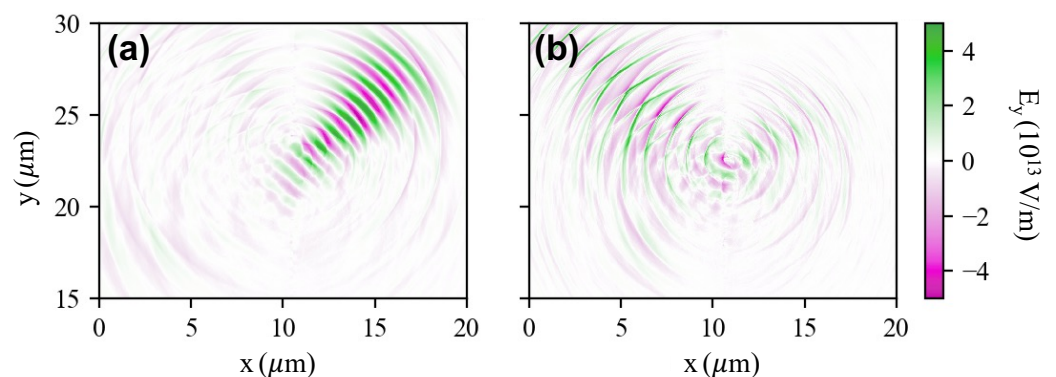


**Figure 10.** Spatial distribution of the transverse electric field  $E_y$  (in  $10^{13} \text{ V m}^{-1}$  units), in the DPM (no-prepulse) laser configuration with a Si target of (a) 10 nm and (b) 20 nm thickness.

The simulated proton energy spectra, for a 200 nm Si + 50 nm Al target (DPM case, red dashed line) and a 1.5  $\mu\text{m}$  Al target (no-DPM case, blue solid line), are plotted alongside the experimental data in Figure 4a. Both simulation curves, integrated over the entire simulation duration (500 fs after peak laser impact), capture well the exponential shape of the distributions as well as their cutoff energies ( $E_{\text{max}} = 32$  MeV and 24 MeV, respectively).

Moreover, the simulated electron spectra, plotted in Figure 4b, indicate that the no-DPM configuration generates hot electrons with energies similar to the DPM case, but in much larger numbers. However, this more energetic electron spectrum in the no-DPM case does not translate into better ion acceleration, as shown in Figure 4a. This counterintuitive observation suggests that the stronger ion acceleration achieved with a DPM has a different origin. As discussed in the following, this could result from an enhanced  $E_x$  field acting on the proton bunch due to sharper density gradients at the time of the laser peak.

To explain the stronger proton acceleration observed at high laser contrast, we plot in Figure 11 the evolution of longitudinal lineouts (across the center of the focal spot) of the particle (electron and proton) densities and electric ( $E_x$  and  $E_y$ ) fields, respectively measured in units of  $n_c$  and  $E_0 = m_e c \omega_0 / e$ . The  $E_x$  field is averaged over the laser cycle. The time origin coincides with the on-target intensity peak. For a 200 nm Si + 50 nm Al target hit by the high-contrast pulse (top row), the accelerating  $E_x$  field seen by the protons (the front of which is located at  $x \simeq 11 \mu\text{m}$ ) reaches a maximum strength of  $\sim 4 E_0$  just after the laser maximum ( $t = 3.5$  fs). This field decays over time (down to  $\sim 0.75 E_0$  at  $t = 55$  fs), but its spatial maximum always coincides with the outer edge of the proton bunch (Figures 11b,c), where the fastest protons reside (see the ion phase-space in Figure 12b). This spatial overlap of the peak electric field and the fastest protons maximizes the acceleration efficiency.

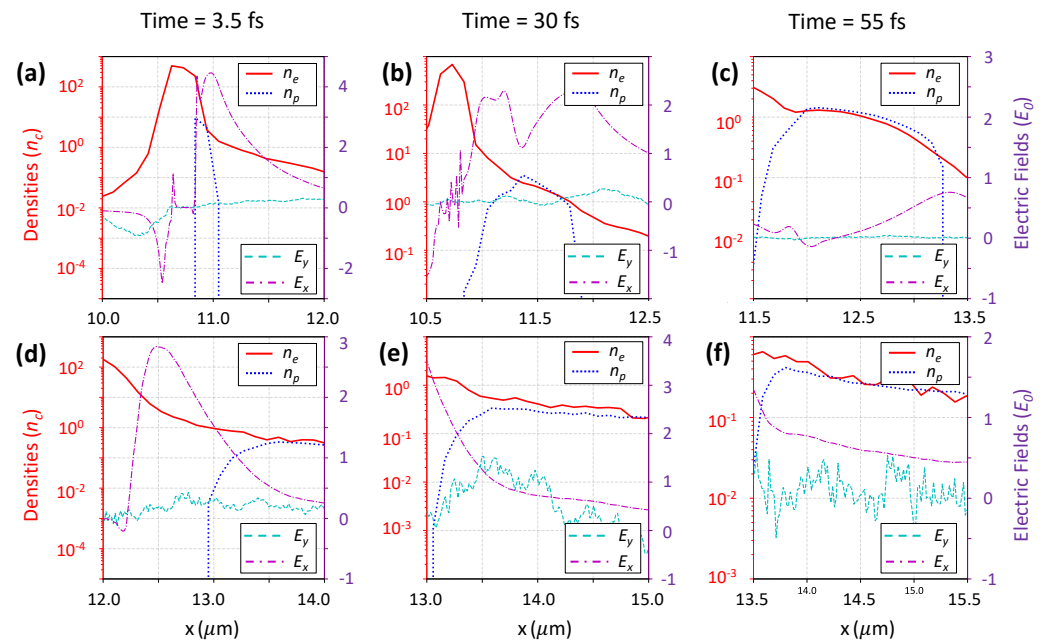


**Figure 11.** Simulations of a DPM shot on a 200 nm Si + 50 nm Al target (a–c) and a direct shot on a 1.5  $\mu\text{m}$  thick Al target (d–f). Longitudinal cuts (across the center of the focal spot at  $y = 21 \mu\text{m}$ ) of the electron density (red solid curves), proton density (blue dotted curves),  $E_y$  electric field (cyan dashed curves) and  $E_x$  (averaged over the laser cycle, purple dotted-dashed curves) are plotted at various times after the laser peak has struck the target ( $t = 0$ ). Particle densities are measured in units of  $n_c$  while field strengths are shown in units of  $E_0 = m_e c \omega_0 / e \simeq 4 \times 10^{12} \text{ V m}^{-1}$ . The target rear side is initially located at  $x = 10.25 \mu\text{m}$  with the DPM and  $x = 11.5 \mu\text{m}$  without it.

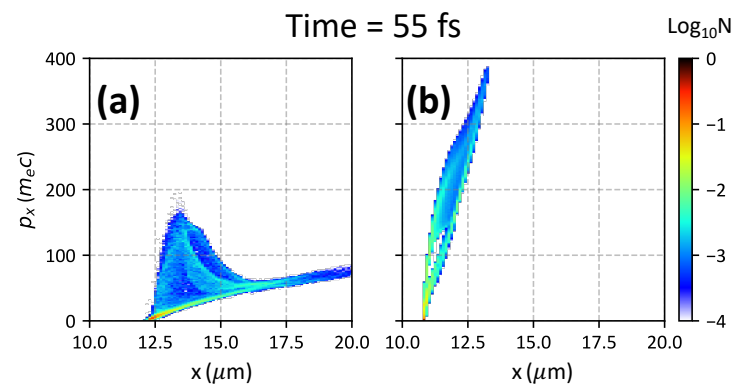


**Figure 12.** Longitudinal ( $x - p_x$ ) phase-space distribution of protons for (a) a direct shot on a 1.5  $\mu\text{m}$  thick Al target and (b) a DPM shot on a 200 nm Si + 50 nm Al target.

The situation is markedly different in the absence of a DPM, for a 1.5  $\mu\text{m}$  thick Al target (bottom row). As shown in Figure 11d, the prepulse-driven expansion of the target backside causes a significant reduction in the  $E_x$  field [64] just after the laser peak ( $E_x \simeq 2.5 E_0$ ). In addition, the spatial maximum of  $E_x$  no longer coincides with the front of the proton bunch (see also Figure 12a).

Another interesting point to notice is the significant  $E_y (>E_0)$  field generated at  $t = 30$  fs after the main pulse irradiation at low laser contrast (Figures 11e and f). This transverse field is mostly positive and hence will bend the protons towards the  $y > 0$  direction, i.e., towards the laser propagation axis [65]. This should contribute to the degraded beam profile seen in Figure 6a, where the high-energy protons show an elongated shape towards the laser axis. On the contrary, at high laser contrast (Figure 11b), the accelerated protons experience a negligible  $E_y$ .

## 5. Conclusions

In summary, we demonstrate significant improvement in proton acceleration from thin solid targets using a double plasma mirror (DPM) [34] to enhance the temporal contrast of the ultrashort (24 fs), ultraintense ( $>10^{21} \text{ W cm}^{-2}$ ) F2 Apollon laser beam. This improvement is observed simultaneously in terms of maximum energy, conversion efficiency, and beam quality. The DPM mitigates the impact of the  $\sim 1$  ps long, relativistic-intensity ( $\sim 10^3$  contrast) laser pulse preceding the main pulse, thereby enabling solid foils as thin as 20 nm to be used. In contrast, the minimum target thickness exploitable under standard irradiation conditions is 800 nm. With the DPM, we were able to accelerate protons up to 15 MeV from a 20 nm thick foil, and achieved a peak proton energy of 35 MeV from a 250 nm foil, with only 5 J of laser energy. Remarkably, this maximum proton energy is  $\sim 40\%$  higher than without the DPM, despite 50% less laser energy. Two-dimensional (2D) PIC simulations attribute the superior performance of the DPM configuration to a stronger effective longitudinal electrostatic field and its closer overlap with the expanding proton bunch when the main laser pulse interacts with the sharp-gradient solid foil. These results pave the way for optimizing laser-driven X-ray and neutron sources [11], opening new perspectives in nuclear material interrogation [13,66–68] and medicine [7]. Furthermore, we can expect even further improvements in laser-proton acceleration at higher intensities, such as with the upcoming 10 PW-scale F1 beam of the Apollon facility.

**Author Contributions:** Conceptualization, J.F.; methodology, J.F., F.M. and A.A.; software, W.Y., Y.Y., P.A., E.d., X.D. and L.G.; investigation, R.L., T.W., J.F., W.Y., I.C., A.B., E.C., C.G., I.P., D.P., D.M. and L.G.; data curation, P.K., F.T., W.Y., J.F., Q.D., E.F., S.P. and R.L.; writing—original draft preparation, W.Y., J.F., R.L., E.F. and L.G.; writing—review and editing, all. All authors have read and agreed to the published version of the manuscript.

**Funding:** This work was supported by funding from the European Research Council (ERC) under the European Unions Horizon 2020 research and innovation program (Grant Agreement No. 787539, Project GENESIS), by CNRS through the MITI interdisciplinary programs and by IRSN through its exploratory research program. The project was also made possible thanks to the credits of the Hubert Curien Maimonides program made available by the French Ministry of Europe and Foreign Affairs and the French Ministry of Higher Education and Research. We acknowledge the financial support of the IdEx University of Bordeaux/Grand Research Program “GPR LIGHT”, and of the Pazy Foundation Grant No. 435/2023. The computational resources of this work were supported by the National Sciences and Engineering Research Council of Canada (NSERC) and Compute Canada (Job: pve-323-ac, PA).

**Institutional Review Board Statement:** Not applicable.

**Informed Consent Statement:** Not applicable.

**Data Availability Statement:** The data that support the findings of this study are available from the corresponding author upon reasonable request.

**Acknowledgments:** The authors acknowledge the national research infrastructure Apollon and the LULI staff for their technical assistance.

**Conflicts of Interest:** Author S.P. was employed by the company HB11. The remaining authors declare that the research was conducted in the absence of any commercial or financial relationships that could be construed as a potential conflict of interest.

## References

1. Daido, H.; Nishiuchi, M.; Pirozhkov, A.S. Review of laser-driven ion sources and their applications. *Rep. Prog. Phys.* **2012**, *75*, 056401. [[CrossRef](#)] [[PubMed](#)]
2. Macchi, A.; Borghesi, M.; Passoni, M. Ion acceleration by superintense laser-plasma interaction. *Rev. Mod. Phys.* **2013**, *85*, 751. [[CrossRef](#)]
3. Zimmer, M.; Scheuren, S.; Ebert, T.; Schaumann, G.; Schmitz, B.; Hornung, J.; Bagnoud, V.; Rödel, C.; Roth, M. Analysis of laser-proton acceleration experiments for development of empirical scaling laws. *Phys. Rev. E* **2021**, *104*, 045210. [[CrossRef](#)] [[PubMed](#)]
4. Schaeffer, D.B.; Bott, A.F.; Borghesi, M.; Flippo, K.A.; Fox, W.; Fuchs, J.; Li, C.; Séguin, F.H.; Park, H.S.; Tzeferacos, P.; et al. Proton imaging of high-energy-density laboratory plasmas. *Rev. Mod. Phys.* **2023**, *95*, 045007. [[CrossRef](#)]
5. Bin, J.; Obst-Huebl, L.; Mao, J.H.; Nakamura, K.; Geulig, L.D.; Chang, H.; Ji, Q.; He, L.; De Chant, J.; Kober, Z.; et al. A new platform for ultra-high dose rate radiobiological research using the BELLA PW laser proton beamline. *Sci. Rep.* **2022**, *12*, 1484. [[CrossRef](#)] [[PubMed](#)]
6. Lelasseux, V.; Söderström, P.A.; Aogaki, S.; Burdonov, K.; Chen, S.; Cvetinovic, A.; Dechefdebien, E.; Dorard, S.; Fazzini, A.; Gremillet, L.; et al. Experimental investigation of the effect of ionization on the 51V (p, n) 51Cr reaction. *arXiv* **2023**, arXiv:2309.16340.
7. Kroll, F.; Brack, F.E.; Bernert, C.; Bock, S.; Bodenstern, E.; Brüchner, K.; Cowan, T.E.; Gaus, L.; Gebhardt, R.; Helbig, U.; et al. Tumour irradiation in mice with a laser-accelerated proton beam. *Nat. Phys.* **2022**, *18*, 316–322. [[CrossRef](#)]
8. Roth, M.; Jung, D.; Falk, K.; Guler, N.; Deppert, O.; Devlin, M.; Favalli, A.; Fernandez, J.; Gautier, D.; Geissel, M.; et al. Bright laser-driven neutron source based on the relativistic transparency of solids. *Phys. Rev. Lett.* **2013**, *110*, 044802. [[CrossRef](#)] [[PubMed](#)]
9. Higginson, D.; Vassura, L.; Gugiu, M.; Antici, P.; Borghesi, M.; Brauckmann, S.; Diouf, C.; Green, A.; Palumbo, L.; Petrascu, H.; et al. Temporal narrowing of neutrons produced by high-intensity short-pulse lasers. *Phys. Rev. Lett.* **2015**, *115*, 054802. [[CrossRef](#)]
10. Kleinschmidt, A.; Bagnoud, V.; Deppert, O.; Favalli, A.; Frydrych, S.; Hornung, J.; Jahn, D.; Schaumann, G.; Tebartz, A.; Wagner, F.; et al. Intense, directed neutron beams from a laser-driven neutron source at PHELIX. *Phys. Plasmas* **2018**, *25*, 053101. [[CrossRef](#)]
11. Lelièvre, R.; Yao, W.; Waltenspiel, T.; Cohen, I.; Beck, A.; Cohen, E.; Michaeli, D.; Pomerantz, I.; Gautier, D.C.; Trompier, F.; et al. A Comprehensive Characterization of the Neutron Fields Produced by the Apollon Petawatt Laser. *arXiv* **2023**, arXiv:2311.12653.
12. Martinez, B.; Chen, S.; Bolaños, S.; Blanchot, N.; Boutoux, G.; Cayzac, W.; Courtois, C.; Davoine, X.; Duval, A.; Horny, V.; et al. Numerical investigation of spallation neutrons generated from petawatt-scale laser-driven proton beams. *Matter Radiat. Extrem.* **2022**, *7*, 024401. [[CrossRef](#)]
13. Yogo, A.; Lan, Z.; Arikawa, Y.; Abe, Y.; Mirfayzi, S.; Wei, T.; Mori, T.; Golovin, D.; Hayakawa, T.; Iwata, N.; et al. Laser-driven neutron generation realizing single-shot resonance spectroscopy. *Phys. Rev. X* **2023**, *13*, 011011. [[CrossRef](#)]
14. Horný, V.; Chen, S.N.; Davoine, X.; Gremillet, L.; Fuchs, J. Quantitative feasibility study of sequential neutron captures using intense lasers. *Phys. Rev. C* **2024**, *109*, 025802. [[CrossRef](#)]

15. Ziegler, T.; Göthel, I.; Assenbaum, S.; Bernert, C.; Brack, F.E.; Cowan, T.E.; Dover, N.P.; Gaus, L.; Kluge, T.; Kraft, S.; et al. Laser-driven high-energy proton beams from cascaded acceleration regimes. *Nat. Phys.* **2024**, 1–6. [[CrossRef](#)]
16. Wilks, S.; Langdon, A.; Cowan, T.; Roth, M.; Singh, M.; Hatchett, S.; Key, M.; Pennington, D.; MacKinnon, A.; Snavely, R. Energetic proton generation in ultra-intense laser–solid interactions. *Phys. Plasmas* **2001**, 8, 542–549. [[CrossRef](#)]
17. Mora, P. Thin-foil expansion into a vacuum. *Phys. Rev. E* **2005**, 72, 056401. [[CrossRef](#)] [[PubMed](#)]
18. Mackinnon, A.; Borghesi, M.; Hatchett, S.; Key, M.; Patel, P.; Campbell, H.; Schiavi, A.; Snavely, R.; Wilks, S.; Willi, O. Effect of plasma scale length on multi-MeV proton production by intense laser pulses. *Phys. Rev. Lett.* **2001**, 86, 1769. [[CrossRef](#)] [[PubMed](#)]
19. McKenna, P.; Ledingham, K.; Yang, J.; Robson, L.; McCanny, T.; Shimizu, S.; Clarke, R.; Neely, D.; Spohr, K.; Chapman, R.; et al. Characterization of proton and heavier ion acceleration in ultrahigh-intensity laser interactions with heated target foils. *Phys. Rev. E* **2004**, 70, 036405. [[CrossRef](#)]
20. Fuchs, J.; Sentoku, Y.; Karsch, S.; Cobble, J.; Audebert, P.; Kemp, A.; Nikroo, A.; Antici, P.; Brambrink, E.; Blazevic, A.; et al. Comparison of laser ion acceleration from the front and rear surfaces of thin foils. *Phys. Rev. Lett.* **2005**, 94, 045004. [[CrossRef](#)]
21. Bolton, P.; Borghesi, M.; Brenner, C.; Carroll, D.; De Martinis, C.; Fiorini, F.; Flacco, A.; Floquet, V.; Fuchs, J.; Gallegos, P.; et al. Instrumentation for diagnostics and control of laser-accelerated proton (ion) beams. *Phys. Med.* **2014**, 30, 255–270. [[CrossRef](#)]
22. Fuchs, J.; Antici, P.; d’Humières, E.; Lefebvre, E.; Borghesi, M.; Brambrink, E.; Cecchetti, C.; Kaluza, M.; Malka, V.; Mancossi, M.; et al. Laser-driven proton scaling laws and new paths towards energy increase. *Nat. Phys.* **2006**, 2, 48–54. [[CrossRef](#)]
23. Dromey, B.; Coughlan, M.; Senje, L.; Taylor, M.; Kuschel, S.; Villagomez-Bernabe, B.; Stefanuik, R.; Nersisyan, G.; Stella, L.; Kohanoff, J.; et al. Picosecond metrology of laser-driven proton bursts. *Nat. Commun.* **2016**, 7, 10642. [[CrossRef](#)]
24. Ma, W.; Kim, I.J.; Yu, J.; Choi, I.W.; Singh, P.; Lee, H.W.; Sung, J.H.; Lee, S.K.; Lin, C.; Liao, Q.; et al. Laser acceleration of highly energetic carbon ions using a double-layer target composed of slightly underdense plasma and ultrathin foil. *Phys. Rev. Lett.* **2019**, 122, 014803. [[CrossRef](#)]
25. Danson, C.N.; Haefner, C.; Bromage, J.; Butcher, T.; Chanteloup, J.C.F.; Chowdhury, E.A.; Galvanauskas, A.; Gizzi, L.A.; Hein, J.; Hillier, D.I.; et al. Petawatt and exawatt class lasers worldwide. *High Power Laser Sci. Eng.* **2019**, 7, e54. [[CrossRef](#)]
26. Stockem Novo, A.; Kaluza, M.; Fonseca, R.; Silva, L. Optimizing laser-driven proton acceleration from overdense targets. *Sci. Rep.* **2016**, 6, 29402. [[CrossRef](#)]
27. Yan, X.; Lin, C.; Sheng, Z.M.; Guo, Z.; Liu, B.; Lu, Y.; Fang, J.; Chen, J. Generating high-current monoenergetic proton beams by a circularly polarized laser pulse in the phase-stable acceleration regime. *Phys. Rev. Lett.* **2008**, 100, 135003. [[CrossRef](#)]
28. Qiao, B.; Zepf, M.; Borghesi, M.; Dromey, B.; Geissler, M.; Karmakar, A.; Gibbon, P. Radiation-pressure acceleration of ion beams from nanofoil targets: The leaky light-sail regime. *Phys. Rev. Lett.* **2010**, 105, 155002. [[CrossRef](#)]
29. Martin, P.; Ahmed, H.; Doria, D.; Cerchez, M.; Hanton, F.; Gwynne, D.; Alejo, A.; Fernández-Tobías, J.; Green, J.; Macchi, A.; et al. Narrow-band acceleration of gold ions to GeV energies from ultra-thin foils. *Commun. Phys.* **2024**, 7, 3. [[CrossRef](#)]
30. Yin, L.; Albright, B.; Hegelich, B.; Bowers, K.J.; Flippo, K.; Kwan, T.; Fernández, J. Monoenergetic and GeV ion acceleration from the laser breakout afterburner using ultrathin targets. *Phys. Plasmas* **2007**, 14, 056706. [[CrossRef](#)]
31. Palaniyappan, S.; Hegelich, B.M.; Wu, H.C.; Jung, D.; Gautier, D.C.; Yin, L.; Albright, B.J.; Johnson, R.P.; Shimada, T.; Letzring, S.; et al. Dynamics of relativistic transparency and optical shuttering in expanding overdense plasmas. *Nat. Phys.* **2012**, 8, 763–769. [[CrossRef](#)]
32. Chou, H.G.J.; Grassi, A.; Glenzer, S.H.; Fiuza, F. Radiation pressure acceleration of high-quality ion beams using ultrashort laser pulses. *Phys. Rev. Res.* **2022**, 4, L022056. [[CrossRef](#)]
33. Rehwald, M.; Assenbaum, S.; Bernert, C.; Brack, F.E.; Bussmann, M.; Cowan, T.E.; Curry, C.B.; Fiuza, F.; Garten, M.; Gaus, L.; et al. Ultra-short pulse laser acceleration of protons to 80 MeV from cryogenic hydrogen jets tailored to near-critical density. *Nat. Commun.* **2023**, 14, 4009. [[CrossRef](#)]
34. Antici, P.; Fuchs, J.; d’Humières, E.; Lefebvre, E.; Borghesi, M.; Brambrink, E.; Cecchetti, C.; Gaillard, S.; Romagnani, L.; Sentoku, Y.; et al. Energetic protons generated by ultrahigh contrast laser pulses interacting with ultrathin targets. *Phys. Plasmas* **2007**, 14, 030701. [[CrossRef](#)]
35. Lévy, A.; Ceccotti, T.; D’Oliveira, P.; Réau, F.; Perdrix, M.; Quéré, F.; Monot, P.; Bougeard, M.; Lagadec, H.; Martin, P.; et al. Double plasma mirror for ultrahigh temporal contrast ultraintense laser pulses. *Opt. Lett.* **2007**, 32, 310–312. [[CrossRef](#)]
36. Schumacher, D.W.; Zingale, A.; Czapla, N.; Nasir, D.; Cochran, G.E.; Poole, P.L. Liquid Crystal Targets and Plasma Mirrors for PW-Class Laser Experiments. In *OSA High-Brightness Sources and Light-Driven Interactions Congress 2020 (EUVXRAY, HILAS, MICS)*; Optica Publishing Group: Washington, DC, USA, 2020. [[CrossRef](#)]
37. Huang, T.; Zhou, C.; Robinson, A.; Qiao, B.; Zhang, H.; Wu, S.; Zhuo, H.; Norreys, P.; He, X. Mitigating the relativistic laser beam filamentation via an elliptical beam profile. *Phys. Rev. E* **2015**, 92, 053106. [[CrossRef](#)]
38. Dollar, F.; Zulick, C.; Matsuoka, T.; McGuffey, C.; Bulanov, S.; Chvykov, V.; Davis, J.; Kalinchenko, G.; Petrov, G.; Willingale, L.; et al. High contrast ion acceleration at intensities exceeding  $10^{21}$  Wcm<sup>-2</sup>. *Phys. Plasmas* **2013**, 20, 056703. [[CrossRef](#)]
39. Speicher, M.; Haffa, D.; Haug, M.A.; Bin, J.; Gao, Y.; Hartmann, J.; Hilz, P.; Kreuzer, C.; Lindner, F.H.; Ostermayr, T.M.; et al. Integrated double-plasma-mirror targets for contrast enhancement in laser ion acceleration. *J. Phys. Conf. Ser.* **2018**, 1079, 012002. [[CrossRef](#)]



40. Neely, D.; Foster, P.; Robinson, A.; Lindau, F.; Lundh, O.; Persson, A.; Wahlström, C.G.; McKenna, P. Enhanced proton beams from ultrathin targets driven by high contrast laser pulses. *Appl. Phys. Lett.* **2006**, *89*, 021502. [[CrossRef](#)]
41. Antici, P.; Fuchs, J.; d’Humières, E.; Robiche, J.; Brambrink, E.; Atzeni, S.; Schiavi, A.; Sentoku, Y.; Audebert, P.; Pépin, H. Laser acceleration of high-energy protons in variable density plasmas. *New J. Phys.* **2009**, *11*, 023038. [[CrossRef](#)]
42. Higginson, A.; Gray, R.; King, M.; Dance, R.; Williamson, S.; Butler, N.; Wilson, R.; Capdessus, R.; Armstrong, C.; Green, J.; et al. Near-100 MeV protons via a laser-driven transparency-enhanced hybrid acceleration scheme. *Nat. Commun.* **2018**, *9*, 724. [[CrossRef](#)]
43. Poole, P.L.; Obst, L.; Cochran, G.E.; Metzkes, J.; Schlenvoigt, H.P.; Prencipe, I.; Kluge, T.; Cowan, T.; Schramm, U.; Schumacher, D.W.; et al. Laser-driven ion acceleration via target normal sheath acceleration in the relativistic transparency regime. *New J. Phys.* **2018**, *20*, 013019. [[CrossRef](#)]
44. Burdonov, K.; Fazzini, A.; Lelasseux, V.; Albrecht, J.; Antici, P.; Ayoul, Y.; Beluze, A.; Cavanna, D.; Ceccotti, T.; Chabanis, M.; et al. Characterization and performance of the Apollon short-focal-area facility following its commissioning at 1 PW level. *Matter Radiat. Extrem.* **2021**, *6*, 064402. [[CrossRef](#)]
45. Dover, N.; Nishiuchi, M.; Sakaki, H.; Kondo, K.; Alkhimova, M.; Faenov, A.Y.; Hata, M.; Iwata, N.; Kiriya, H.; Koga, J.; et al. Effect of small focus on electron heating and proton acceleration in ultrarelativistic laser-solid interactions. *Phys. Rev. Lett.* **2020**, *124*, 084802. [[CrossRef](#)]
46. Rusby, D.; Kemp, A.; Wilks, S.; Miller, K.; Sherlock, M.; Chen, H.; Simpson, R.; Mariscal, D.; Swanson, K.; Djordjević, B.; et al. Review and meta-analysis of electron temperatures from high-intensity laser–solid interactions. *Phys. Plasmas* **2024**, *31*, 040503. [[CrossRef](#)]
47. Coury, M.; Carroll, D.; Robinson, A.; Yuan, X.; Brenner, C.; Burza, M.; Gray, R.; Quinn, M.; Lancaster, K.; Li, Y.; et al. Influence of laser irradiated spot size on energetic electron injection and proton acceleration in foil targets. *Appl. Phys. Lett.* **2012**, *100*, 074105. [[CrossRef](#)]
48. Badziak, J.; Antici, P.; Fuchs, J.; Jabłoński, S.; Mancic, A.; Parys, P.; Rosiński, M.; Suchańska, R.; Szydlowski, A.; Wołowski, J. Laser-induced generation of ultraintense proton beams for high energy-density science. In *AIP Conference Proceedings*; American Institute of Physics: College Park, MD, USA, 2008; Volume 1024, pp. 63–77.
49. Mirza, I.; Bulgakova, N.M.; Tomáščík, J.; Michálek, V.; Haderka, O.; Fekete, L.; Mocek, T. Ultrashort pulse laser ablation of dielectrics: Thresholds, mechanisms, role of breakdown. *Sci. Rep.* **2016**, *6*, 39133. [[CrossRef](#)]
50. Burdonov, K.; Lelièvre, R.; Forestier-Colleoni, P.; Ceccotti, T.; Cuciuc, M.; Lancia, L.; Yao, W.; Fuchs, J. Absolute calibration up to 20 MeV of an online readout CMOS system suitable to detect high-power lasers accelerated protons. *Rev. Sci. Instrum.* **2023**, *94*, 083303. [[CrossRef](#)]
51. Henig, A.; Steinke, S.; Schnürer, M.; Sokollik, T.; Hörlein, R.; Kiefer, D.; Jung, D.; Schreiber, J.; Hegelich, B.; Yan, X.; et al. Radiation-pressure acceleration of ion beams driven by circularly polarized laser pulses. *Phys. Rev. Lett.* **2009**, *103*, 245003. [[CrossRef](#)]
52. Kar, S.; Kakolee, K.; Qiao, B.; Macchi, A.; Cerchez, M.; Doria, D.; Geissler, M.; McKenna, P.; Neely, D.; Osterholz, J.; et al. Ion acceleration in multispecies targets driven by intense laser radiation pressure. *Phys. Rev. Lett.* **2012**, *109*, 185006. [[CrossRef](#)]
53. Brenner, C.M.; Robinson, A.; Markey, K.; Scott, R.; Gray, R.; Rosinski, M.; Deppert, O.; Badziak, J.; Batani, D.; Davies, J.; et al. High energy conversion efficiency in laser-proton acceleration by controlling laser-energy deposition onto thin foil targets. *Appl. Phys. Lett.* **2014**, *104*, 081123. [[CrossRef](#)]
54. Wagner, F.; Bedacht, S.; Bagnoud, V.; Deppert, O.; Geschwind, S.; Jaeger, R.; Ortner, A.; Tebartz, A.; Zielbauer, B.; Hoffmann, D.; et al. Simultaneous observation of angularly separated laser-driven proton beams accelerated via two different mechanisms. *Phys. Plasmas* **2015**, *22*, 063110. [[CrossRef](#)]
55. Zhuo, W.; Liu, W.; Huang, G.; Zhu, G.; Ma, G. Comparisons of dosimetric properties between GD-300 series of radiophotoluminescent glass detectors and GR-200 series of thermoluminescent detectors. *Nucl. Sci. Tech.* **2007**, *18*, 362–365.
56. Faenov, A.Y.; Pikuz, S.A.; Erko, A.I.; Bryunetkin, B.A.; Dyakin, V.M.; Ivanenkov, G.V.; Mingaleev, A.R.; Pikuz, T.A.; Romanova, V.M.; Shelkovenko, T.A. High-performance X-ray spectroscopic devices for plasma microsources investigations. *Phys. Scr.* **1994**, *50*, 333–338. [[CrossRef](#)]
57. Vyskočil, J.; Klimo, O.; Weber, S. Simulations of bremsstrahlung emission in ultra-intense laser interactions with foil targets. *Plasma Phys. Controll. Fusion* **2018**, *60*, 054013. [[CrossRef](#)]
58. Ryazantsev, S.N.; Martynenko, A.S.; Sedov, M.V.; Skobelev, I.Y.; Mishchenko, M.D.; Lavrinenko, Y.S.; Baird, C.D.; Booth, N.; Durey, P.; Döhl, L.N.; et al. Absolute keV X-ray yield and conversion efficiency in over dense Si sub-petawatt laser plasma. *Plasma Phys. Controll. Fusion* **2022**, *64*, 105016. [[CrossRef](#)]
59. Chen, M.; Sheng, Z.M.; Zheng, J.; Ma, Y.Y.; Bari, M.; Li, Y.T.; Zhang, J. Surface electron acceleration in relativistic laser-solid interactions. *Opt. Express* **2006**, *14*, 3093. [[CrossRef](#)]
60. Serebryakov, D.; Nerush, E.; Kostyukov, I.Y. Near-surface electron acceleration during intense laser–solid interaction in the grazing incidence regime. *Phys. Plasmas* **2017**, *24*, 123115. [[CrossRef](#)]
61. Thévenet, M.; Leblanc, A.; Kahaly, S.; Vincenti, H.; Vernier, A.; Quéré, F.; Faure, J. Vacuum laser acceleration of relativistic electrons using plasma mirror injectors. *Nat. Phys.* **2016**, *12*, 355–360. [[CrossRef](#)]
62. Chung, H.K.; Chen, M.H.; Morgan, W.L.; Ralchenko, Y.; Lee, R.W. FLYCHK: Generalized population kinetics and spectral model for rapid spectroscopic analysis for all elements. *High Energy Density Phys.* **2005**, *1*, 3–12. [[CrossRef](#)]

63. Derouillat, J.; Beck, A.; Pérez, F.; Vinci, T.; Chiamello, M.; Grassi, A.; Flé, M.; Bouchard, G.; Plotnikov, I.; Aunai, N.; et al. Smilei: A collaborative, open-source, multi-purpose particle-in-cell code for plasma simulation. *Comput. Phys. Commun.* **2018**, *222*, 351–373. [[CrossRef](#)]
64. Grismayer, T.; Mora, P. Influence of a finite initial ion density gradient on plasma expansion into a vacuum. *Phys. Plasmas* **2006**, *13*, 032103. [[CrossRef](#)]
65. Horný, V.; Burdonov, K.; Fazzini, A.; Lelasseux, V.; Antici, P.; Chen, S.N.; Ciardi, A.; Davoine, X.; d’Humières, E.; Gremillet, L.; et al. A “lighthouse” laser-driven staged proton accelerator allowing for ultrafast angular and spectral control. *arXiv* **2024**, arXiv:2404.11321.
66. Favalli, A.; Aymond, F.; Bridgewater, J.S.; Croft, S.; Deppert, O.; Devlin, M.J.; Falk, K.; Fernandez, J.C.; Gautier, D.C.; Gonzales, M.A.; et al. *Nuclear Material Detection by One-Short-Pulse-Laser-Driven Neutron Source*; Technical Report; Los Alamos National Lab. (LANL): Los Alamos, NM, USA, 2015.
67. Favalli, A.; Guler, N.; Henzlova, D.; Croft, S.; Falk, K.; Gautier, D.C.; Ianakiev, K.D.; Iliev, M.; Palaniyappan, S.; Roth, M.; et al. Characterizing laser-plasma ion accelerators driving an intense neutron beam via nuclear signatures. *Sci. Rep.* **2019**, *9*, 2004. [[CrossRef](#)]
68. Yogo, A.; Mirfayzi, S.R.; Arikawa, Y.; Abe, Y.; Wei, T.; Mori, T.; Lan, Z.; Hoonoki, Y.; Golovin, D.O.; Koga, K.; et al. Single shot radiography by a bright source of laser-driven thermal neutrons and X-rays. *Appl. Phys. Express* **2021**, *14*, 106001. [[CrossRef](#)]

**Disclaimer/Publisher’s Note:** The statements, opinions and data contained in all publications are solely those of the individual author(s) and contributor(s) and not of MDPI and/or the editor(s). MDPI and/or the editor(s) disclaim responsibility for any injury to people or property resulting from any ideas, methods, instructions or products referred to in the content.